Analysis of shear rate inside a concrete truck mixer

Jon Elvar Wallevik[a,*], Olafur Haralds Wallevik[b]

[a]ICI Rheocenter, Innovation Center Iceland, Arleynir 2, Reykjavik IS-112, Iceland
[b]ICI Rheocenter, Reykjavik University and Innovation Center Iceland, Arleynir 2, Reykjavik IS-112, Iceland

ARTICLE INFO

ABSTRACT

In addition to the mixing energy applied to the fresh concrete (i.e. shearing during mixing), the shear history after mixing is also important. This applies especially to binder rich concretes like the different types of high performance concrete (HPC). With this in mind, the shear rate is analyzed inside a drum of a concrete truck mixer. The objective is to better understand the effect of transport of fresh concrete, from the ready mix plant to the building site. The analysis reveals the effect of different drum charge volume and drum rotational speed. Also, the effect of yield stress and plastic viscosity is investigated. The work shows that the shear rate decreases in an exponential manner with increasing drum charge volume. It is also shown that for a given drum speed, the shear rate decreases both with increasing plastic viscosity and yield stress.

1. Introduction

1.1. Background

Since civilizations first started to build, the human race has sought materials that bind stones into solid formed mass. After the discovery of Portland cement in 1824 (year of patent), concrete has become the most commonly used structural material in modern civilizations. The quality of the concrete structure is of course dependent on the quality of each constituent used in the concrete mix. However, this is not the only controlling factor. The quality also depends very much on the rheological properties of the fresh concrete during placement into the formwork [1]. That is, the concrete must be able to properly flow into all corners of the mold or formwork to fill it completely, with or without external consolidation depending on workability class. Tragic events may sometimes be traced back to concrete of unsuitable consistency resulting in, for example, coldjoint and honeycombing. Therefore, one of the primary criteria for a good concrete structure is that the fresh concrete exhibits satisfactory rheological properties during casting [1]. The use of simulation of flow to analyze such behavior is something that has been increasing in popularity for the last decade [2–9]. In 2014, a RILEM state-of-the art report (TC 222-SCF) was made specifically on this subject [10]. Here, such method is used to analyze the shear rate inside a concrete truck mixer for a wide range of cases. Previously

in [11], such simulation was reported for the case of yield stress 50Pa and plastic viscosity 50Pa·s, in which the aim was to verify a special truck mixer simulator.

1.2. Shear rate condition during transport

In addition to the energy applied during mixing (i.e. shearing during mixing) [12–14], the shear history after mixing is also important [15–17]. This applies especially for binder rich concretes like the (rich) high performance concrete (HPC). This is due to the influence that the binder exerts on the concrete as a whole in terms of thixotropic- and structural breakdown behavior (these two terms are well explained in [18]). The rheological state of the binder depends heavily on the shear rate and especially on its history [15–17]. That is, in a highly agitated system (high shear rate), the cement particles will disperse, making the overall fresh concrete more flowable. While in a slowly agitated system, the cement particles will coagulate and thus thicken the overall fresh concrete.

The rheological properties of the fresh concrete depends on the proportions of each constituent as well as on their quality. However, as is apparent from the above paragraph, conditions like the shear rate during transport can play a major role on final workability. That is, a concrete batch with seemingly target rheological behavior at the ready mix plant can become unsuitable at the building site due to thixotropic thickening, caused by insufficient agitation during transport (i.e. low shear rate). The decrease in the slump during transport in truck mixer can be up to 90mm, which corresponds to a deviation of one and a half consistency class [11]. Such could lead to the refusal

of acceptance, or in the case of acceptance, make successful casting in awkward sections or through congested reinforcement difficult, resulting for example in honeycombing [1,11].

1.3. Concrete truck mixer

In this work, the shear rate is analyzed inside the drum of a concrete truck mixer. This is done to better understand the potential effect of transport, from the ready mix plant to the building site, in terms of the concrete final rheological state. From Section 1.2, a higher shear rate will imply increased dispersion of the cement particles and thus more flowable concrete during the casting phase. Likewise, a lower shear rate will imply insufficient agitation, increased thixotropic rebuild and thus stiffer concrete during casting.

Because the shear rate within the drum is highly non-uniform and time dependent, meaning $\dot{\gamma} = \dot{\gamma}(x, y, z, t)$, a two step integration is most necessary to generate quantifiable values for analysis and comparison, which is shown later. The final outcome is given by $\dot{\gamma}_t$ and is simply referred to as "shear rate". Here, this shear rate is analyzed as a function of drum rotational speed $f = 0.03, 0.07, 0.11, 015, 019$ and 0.23rps (revolutions per second) and drum charge volume $V = 2.6\text{m}^3, 5.4\text{m}^3$ and 8.2m^3. In addition to this, the effect of yield stress $\tau_0 = 0, 150$ and 300Pa and plastic viscosity $\mu = 25, 75$ and 125Pa·s, is analyzed.

1.4. Software

The simulation software used in this work is the OpenFOAM. It is licensed under the GNU General Public License (GNU GPL) and available at http://openfoam.org, without charge or annual fee of any kind. The benefits of using a GNU GPL licensed code rather than a closed commercial code, is that the user has always a full access to the source code, without any restriction, either to understand, correct, modify or enhance the software. Here, this is a highly desirable feature since a custom made solver is used for the current analysis. The software OpenFOAM is written in C++. As such, an object-oriented programming approach is used in the creation of data types (fields) that closely mimics those of mathematical field theory [19]. For the code parallelization and communication between processors, the domain decomposition method is used with the Message Passing Interface, or MPI [20]. In OpenFOAM, the collocated mesh system (in Cartesian coordinates) is applied in conjunction with the finite volume method (FVM).

2. Experimental setup

2.1. Geometry and mesh of the drum

The geometry under consideration is a market-leading commercially available concrete drum, produced in Germany. Its geometry is shown in Fig. 1. The total drum volume is 15.7m³, but the max rated drum capacity is 9m³. The max drum diameter is 2.3m, while its length is about 5.2m. Since a small end part of the actual drum is not included in the mesh, the drum volume in Fig. 1 is 15m³, and not 15.7m³. More precisely, 41.5cm is cut off the drum rear part (i.e. where the hopper is). Since this part is never occupied by concrete for the current analysis, it will not affect the results. The nominal range of drum speed is between 0 and 14rpm (i.e. from 0 to 0.23rps). The inclination of the drum relative to the horizontal is 11°.

The mesh in Fig. 1 is generated with a native OpenFOAM mesh utility called blockMesh. To investigate the mesh dependency of the numerical result, two different mesh densities (or mesh resolutions) are used, namely 58,888 and 372,568 cells, which are shown in the left and right illustrations of Fig. 1, respectively. For the former case, 88% of the cells are hexahedra, while it is 99% for the latter case. In either case, the remaining cells consist of prisms, tetrahedra and
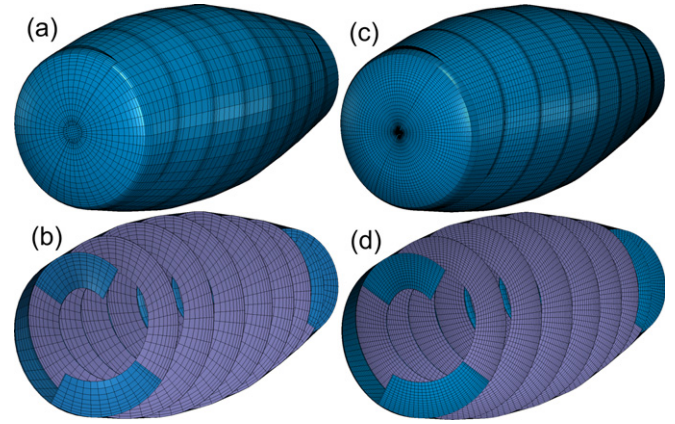

Fig. 1. Finite volume mesh of the drum, 58,888 cells (to the left) and 372,568 cells (to the right).

polyhedra. In the end of the mesh generation, its quality is checked with another native OpenFOAM utility, named checkMesh.

The internal dimensions shown to the left and right in Fig. 1 are identical and were directly measured at the local concrete premixing plant: the internals consists of two helix shaped blades, in which the blade thickness is roughly 8mm, while the height is about 430mm. The space between two adjacent blades is 620mm on the average. As shown in Fig. 1, all these numbers vary as a function of the location within the drum. These number also change as a function of time, depending on drum usage. That is, the concrete wears and tears the internals of the drum with time.

2.2. Volume of fluid (VOF)

For the current analysis, it is important to divide the drum content between the atmospheric air and the fresh concrete. This is done with a so-called *free interface*. Numerical methods that can manage such division are classified into two groups depending on the fundamental type of mesh used [21]: these are moving mesh (Lagrangian mesh) and fixed mesh (Eulerian mesh). Although the moving mesh approach allows a sharp interface definition it encounters serious problems in cases when the interface undergoes large deformations where the moving mesh may become severely distorted [20]. Because of this, the Eulerian mesh approach is preferred in many cases, like the volume-of-fluid [22], the level set [21,23] or the marker and cell [23] methods. In this work, the volume-of-fluid method (VOF) is used and thus the text that now follows is relative to that specific theory.

Here, the volume fraction (also, solid concentration or phase volume) of fresh concrete within each computational cell is represented with α_1, while the volume fraction of atmospheric air is represented with α_2. More precisely, $\alpha_1 = V_c/V_{cell}$, where V_{cell} is the volume of the cell and V_c is the volume of concrete within the cell (i.e. $V_c \leq V_{cell}$). When $\alpha_1 = 1$, the computational cell is filled only with fresh concrete, while if $\alpha_1 = 0$, the cell is filled only with atmospheric air. For the interface between air and concrete, the following applies $0 < \alpha_1 < 1$. In general, the value of α_1 can range from 0 to 1. In this text, the fresh concrete (α_1) will also have standard VOF designations like *phase 1* or *fluid 1*. The same applies for the atmospheric air (α_2), i.e. *phase 2* or *fluid 2*.

The mixed fluid properties density ρ and apparent viscosity η are weighted by the volume fractions α_1 and α_2 of the two fluids given by Eqs. (1) and (2) [24,25]

$$\rho = \rho_1 \, \alpha_1 + \rho_2 \, \alpha_2, \tag{1}$$

$$\eta = \eta_1 \, \alpha_1 + \eta_2 \, \alpha_2. \tag{2}$$

In each and every computational cell, the following is always valid $\alpha_1 + \alpha_2 = 1$, meaning if the quantity of phase 1 is known by α_1, then so is the quantity of phase 2 by $\alpha_2 = 1 - \alpha_1$. This means it is sufficient to calculate only the interface advection for α_1. This interface is moved through a fixed mesh and is captured by a *phase transport equation*. Relative to this specific equation, the VOF can be divided between two families, namely the *direct methods* and the *reconstruction methods* [24]. For the latter approach, the phase transport equation is approximated typically in two steps, first by a geometric interface reconstruction step and thereafter by an interface propagation step [24]. Examples of such approaches are the PLIC [26] and SLIC [27].

Unlike geometric interface reconstruction methods, the *direct methods* do not introduce geometrical representation of the interface, but rather try to maintain sharply defined interface by properly chosen discretization scheme, commonly known as *compressive differencing scheme* [28]. Example of such are the CICSAM [29,30] and HRIC [31]. Another method, which could be considered to belong to the *direct methods* is the so-called Weller-scheme [32,33]. However, instead of using compressive differencing scheme like done in CICSAM, the compression of the interface is achieved by applying an extra compression term directly into the phase transport equation [23,33]. This approach is used here and thus better explained below.

2.3. Phase transport equation

The transport equation of each volume fraction α_1 and α_2 in a incompressible two-fluid system is given by Eq. (3), where $i = 1, 2$ [24]

$$\frac{\partial \alpha_i}{\partial t} + \nabla \cdot (\alpha_i \, \mathbf{U}_i) = 0. \tag{3}$$

However, with $\alpha_2 = 1 - \alpha_1$, it is sufficient to consider the transport equation of α_1 only. Therefore, with $i = 1$, Eq. (3) gives:

$$\frac{\partial \alpha_1}{\partial t} + \nabla \cdot (\alpha_1 \, \mathbf{U}_1) = 0. \tag{4}$$

To solve this transport equation, the velocity of phase 1 is needed, namely $\mathbf{U}_1$. In the much used original VOF method by Hirt and Nichols [22], the velocity $\mathbf{U}_1$ is assumed to be equal to the mixed velocity $\mathbf{U} = \alpha_1 \mathbf{U}_1 + \alpha_2 \mathbf{U}_2$ [24]. This is only valid if α_1 is maintained as a step function throughout the domain, for example, numerical diffusion at the interface is not allowed [24]. Strictly speaking, this assumption is generally not valid. However, with the mixed velocity $\mathbf{U} = \alpha_1 \mathbf{U}_1 + \alpha_2 \mathbf{U}_2 = \alpha_1 \mathbf{U}_1 + (1 - \alpha_1) \mathbf{U}_2$ and the relative velocity between the phases $\mathbf{U}_r = \mathbf{U}_1 - \mathbf{U}_2$, it is possible to convert $\mathbf{U}_1$ over to $\mathbf{U}$ [32,33]. That is, by adding together $\alpha_1 \mathbf{U} = \alpha_1^2 \mathbf{U}_1 + \alpha_1 (1 - \alpha_1) \, \mathbf{U}_2$ and $\alpha_1 (1 - \alpha_1) \mathbf{U}_r = \alpha_1 (1 - \alpha_1)(\mathbf{U}_1 - \mathbf{U}_2)$, it can be shown after few steps that $\alpha_1 \mathbf{U}_1 = \alpha_1 \mathbf{U} + \mathbf{U}_r \alpha_1 (1 - \alpha_1)$ [24]. With this result, Eq. (4) can be converted to Eq. (5).

$$\frac{\partial \alpha_1}{\partial t} + \nabla \cdot (\alpha_1 \, \mathbf{U}) + \nabla \cdot (\mathbf{U}_r \, \alpha_1 \, (1 - \alpha_1)) = 0. \tag{5}$$

The term $\mathbf{U}_r$ is a velocity field suitable to compress the interface [33]. With the multiplication term $\alpha_1 (1 - \alpha_1)$, the compression term $\mathbf{U}_r \alpha_1 (1 - \alpha_1)$ is only active in the thin interface region, between the fresh concrete and the atmospheric air $0 < \alpha_1 < 1$.

One of the critical issues with Eq. (5) is the discretization of the advection term $\nabla \cdot (\alpha_1 \mathbf{U})$. Lower order schemes like the first order upwind method smear the interface due to numerical diffusion and higher order schemes are unstable, resulting in numerical oscillations [23]. Thus, it is necessary to apply special advection schemes that can contribute to a sharper interface and produce better monotonic profiles of the volume fraction α_1 [23]. To do this, the Flux Corrected Transport technique (FCT) is applied, which was introduced by Boris and Book [34] and later enhanced by Zalesak [35]. OpenFOAM implementation of FCT is named MULES (Multidimensional Universal Limiter for Explicit Solution) [36]. It is based on a similar concept relative to Zalesak's limiter λ, but its determination is iterative [36].

The FCT can be considered to be a *compressive differencing scheme* and thus has been used on Eq. (4), with $\mathbf{U}_1 = \mathbf{U}$, to maintain a sharp interface [23]. Therefore, with the special compression term in Eq. (5) and with the use of MULES (i.e. FCT), a double compression is being applied. Here, the FCT is applied on both advection terms in Eq. (5).

2.4. Governing equation

For non-Newtonian fluids, like what applies for cement based materials, the governing equation is the Cauchy equation of motion, given by Eq. (6) [37,38]. Being a "parent" of the Navier–Stokes equations, the Cauchy equation is also fully valid for Newtonian fluids like the atmospheric air.

$$\left(\frac{\partial \rho \mathbf{U}}{\partial t} \right) + \nabla \cdot (\rho \, \mathbf{U}\mathbf{U}) + \mathbf{F}_{\mathrm{cor}} + \mathbf{F}_{\mathrm{cen}} = -\nabla p + \nabla \cdot \mathbf{T} + \rho \, \mathbf{g} + \mathbf{F}_s. \tag{6}$$

Since the VOF method is a single pressure system [20], the pressure p in Eq. (6) is not calculated separately for each of the phases α_1 and α_2 (i.e. for concrete and air). The same applies for the velocity $\mathbf{U}$, which is strictly speaking equal to $\alpha_1 \mathbf{U}_1 + \alpha_2 \mathbf{U}_2$. That is, the mixed velocity $\mathbf{U}$ is solved as a single identity by Eq. (6). Furthermore, the pressure p is substituted by a modified version of it, namely $p^* = p - \rho \mathbf{g} \cdot \mathbf{x}$ [33], where the term $\mathbf{x}$ is the vector location of the corresponding fluid particle. The implications and benefits of the modified pressure p^* is well explained in [20,24,33].

The density ρ in Eq. (6) is given by Eq. (1), the term t represents the time and $\mathbf{g}$ is the gravity. The term $\mathbf{F}_s$ is the force by surface tension between the two phases α_1 and α_2 (concrete and air), and is calculated in accordance with the Continuum-Surface-Force (CSF) model of Brackbill et al. [39]. A good introductory text about CSF is given in [29] and thus not repeated here. The terms $\mathbf{F}_{\mathrm{cor}}$ and $\mathbf{F}_{\mathrm{cen}}$ will be explained later in Section 2.6, while the extra stress tensor $\mathbf{T}$ is dealt with in Section 2.5.

In addition to Eq. (6), the continuity equation for an incompressible fluid $\nabla \cdot \mathbf{U} = 0$ is used to generate the so-called pressure equation, which is used in calculating the pressure distribution $p^* = p^*(x, y, z, t)$, see [24,40].

2.5. Constitutive equation

The constitutive equation consists of the Generalized Newtonian Model [41], or in short GNM and is given by $\mathbf{T} = 2 \, \eta \, \dot{\boldsymbol{\varepsilon}}$ [42]. The term $\dot{\boldsymbol{\varepsilon}} = \frac{1}{2}(\nabla \mathbf{U} + (\nabla \mathbf{U})^{\mathrm{T}})$ is known as the rate-of-deformation tensor [37,38]. Here, the apparent viscosity η by is given by Eq. (2), in which the fresh concrete (i.e. phase 1) is modeled as a Bingham viscoplastic fluid $\eta_1 = \mu + \tau_0/\dot{\gamma}$, while the atmospheric air (i.e. phase 2) as a Newtonian fluid $\eta_2 = $ constant. The computational implementation of η_1 into the source code is carried out through the regularization approach [43–49].

2.6. Flow in a rotating reference frame

The range of angular velocity $\boldsymbol{\omega}$ for the concrete drum under consideration is between 0 and 1.46 rad/s (i.e. $f = |\boldsymbol{\omega}|/(2\pi)$ from 0 to

0.23rps). This rotation is included into the analysis by using a so-called single reference frame (SRF) approach [50]. This means that the computational mesh in Fig. 1 is kept stationary, while the gravity field $\mathbf{g}$ is rotated at a given constant angular velocity $\boldsymbol{\omega}$. In other words, instead of having a rotating drum on a stationary Earth, the drum is stationary and the Earth is rotated around it. However in taking this step, the computational domain represents no longer an inertial reference frame [51]. With this, the Coriolis force $\mathbf{F}_{cor} = 2\rho\boldsymbol{\omega} \times \mathbf{U}$ and the centrifugal force $\mathbf{F}_{cen} = \rho\boldsymbol{\omega} \times (\boldsymbol{\omega} \times \mathbf{x})$ have to be included into the governing equation as already shown with Eq. (6) [51]. Except for $\boldsymbol{\omega}$, all variables (i.e. α_1, $\dot{\gamma}$, $\mathbf{U}$, p^*) are now relative to the non-inertial (i.e. rotating) reference frame. In this framework, a scalar equation like Eq. (5) remains unchanged [51]. Furthermore, scalar quantities like ρ, α_1, $\dot{\gamma}$, $\dot{\gamma}_t$, V or p^* appear the same in inertial and non-inertial reference frames, as does their material derivative [51]. However, for a vector quantity like the velocity $\mathbf{U}$, the transformation between the two reference frames is $\mathbf{U}_{in} = \mathbf{U} + \boldsymbol{\omega} \times \mathbf{x}$, where $\mathbf{U}_{in}$ is the inertial velocity [51].

2.7. Boundary conditions

For the velocity $\mathbf{U}$, the no-slip boundary condition (i.e. the Dirichlet boundary condition) is used at all solid wall boundaries, meaning $\mathbf{U}|_b = 0$, where b is an acronym for boundary. The justification for the no-slip boundary condition is by the roughness present inside the drum. This is due to the tear and wear of the concrete on the steel surface. Surface roughness is also present by the hardened concrete stuck on the interior as shown in the right illustration of Fig. 2. Correct or not, the results shown in this work are relative to this assumption.

At wall boundaries, the Neumann boundary condition is applied for the volume fraction of concrete α_1, given by $\partial\alpha_1/\partial\mathbf{n}|_b = \mathbf{n}\cdot\nabla\alpha_1|_b = 0$. This means that surface tension is not influencing the movement of the free interface at the boundary. This is a reasonable assumption for systems of large dimensions like what applies in this work. For the modified pressure p^*, its boundary condition is basically set as $\partial p^*/\partial\mathbf{n}|_b = 0$.

2.8. Solution algorithm

A custom made solver is used in this work named interDrumFoam, which is based on the standard solver *interFoam*. For the former, Eqs. (6) and (5) as well as the continuity equation (see Section 2.4), are solved in parallel to obtain the velocity $\mathbf{U}$ and pressure p^* profiles throughout the geometry. More precisely, the pressure velocity coupling is handled with a combination of the SIMPLE [52] and the PISO [52] algorithms (the combination is designated PIMPLE), using a modified Rhie–Chow interpolation for cell

centered data storage [40]. Relative to the solver, the PIMPLE consists of the following steps: (A) set up the phase transport equation Eq. (5) and solve it; (B) set up the discretized momentum predictor Eq. (6) with relaxation; (C) solve the discretized momentum predictor (an optional step); (D) compute the cell face fluxes $\phi = \mathbf{U}\cdot\mathbf{S}$ (the term $\mathbf{S}$ is the face area vector of a cell [53]); (E) solve the pressure equation (for p^*); (F) correct and adjust the flux ϕ at cell faces in such manner that it is guaranteed conserved; (G) apply under relaxation to the pressure field p^*; (H) correct the velocity $\mathbf{U}$ on the basis of the new (relaxed) pressure field; (I) update the boundary conditions; (J) repeat until the convergence criteria are satisfied. (K) Move on to the next time step.

3. Data analysis

For 3D incompressible flow where the GNM is valid (Section 2.5), it can be shown that the shear rate $\dot{\gamma}$ is correctly calculated by [54]

$$\dot{\gamma} = \sqrt{2\,\dot{\boldsymbol{\varepsilon}} : \dot{\boldsymbol{\varepsilon}}}. \tag{7}$$

Because the shear rate $\dot{\gamma} = \dot{\gamma}(x,y,z,t)$ by Eq. (7) within the concrete sample is highly non-uniform and time dependent, a volume averaged shear rate is most necessary to generate quantifiable values for analysis and comparison. This integration is given by Eq. (8).

$$\bar{\dot{\gamma}}(t) = \frac{1}{V}\int_V \dot{\gamma}(x,y,z,t)\,dV. \tag{8}$$

The term V is the volume of the concrete sample inside the drum. The drum charge volume V is nominally equal to either 2.6m^3, 5.4m^3 or 8.2m^3. However, the actual value of V and used in Eq. (8), will deviate slightly from nominal values, depending on how much becomes stuck on the drum steel boundary. More precisely, the concrete that becomes stuck on the solid boundary inside the drum, on the atmospheric air side, is not included in Eq. (8).

Fig. 3 shows an example of the shear rate $\bar{\dot{\gamma}}(t)$ by Eq. (8) plotted as a function of time t for the two cases of drum charge volume 2.6m^3 (to the left) and 8.2m^3 (to the right) and different drum speed f. Above each plot is shown an example of the drum with the corresponding quantity of concrete, in which the clearly visible surface marks the boundary between the air (above) and the concrete (below). In these top illustrations are cross sections of shear rate $\dot{\gamma}$ by Eq. (7), where the shown color range demonstrates the non-uniformity of the shear rate, thus making the integration in Eq. (8) most necessary to generate quantifiable values for analysis and comparison. As already indicated by this equation, the shear rate of the atmospheric air is never included into the current analysis, as such is not relevant.

The results shown in Fig. 3, apply to the more computational challenging cases, namely when the yield stress is $\tau_0 = 300$Pa, and the plastic viscosity is $\mu = 75$Pa·s. The density of the concrete samples is set as $\rho_1 = 2350$kg/m^3 in this figure and applies to all other cases in this work.

At the start of each simulation in Fig. 3, the concrete sample is stationary and therefore the shear rate $\bar{\dot{\gamma}}(t)$ by Eq. (8) begins at 0s^{-1}. At the start of rotation, there is some wave generation occurring due to the fact that the concrete sample is interacting with the helical shape of the mixing blades inside the drum. Depending on Bingham values τ_0 and μ, drum charge volume V and drum rotational speed f, these wave phenomenon will differ. Height and distance between the helically shaped blades and the overall drum geometry will most certainly also influence the waves.

For the lower drum speed like $f = 0.03$rps, the simulation time of 20 s will only rotate the drum by the angle of $(2\pi f)\cdot 20s = 260°$, or just above half a revolution. One might expect an incomplete shear

Fig. 2. Inside the drum, which is simulated in this work. The picture is taken during internal measurement for the meshing phase done in Fig. 1.
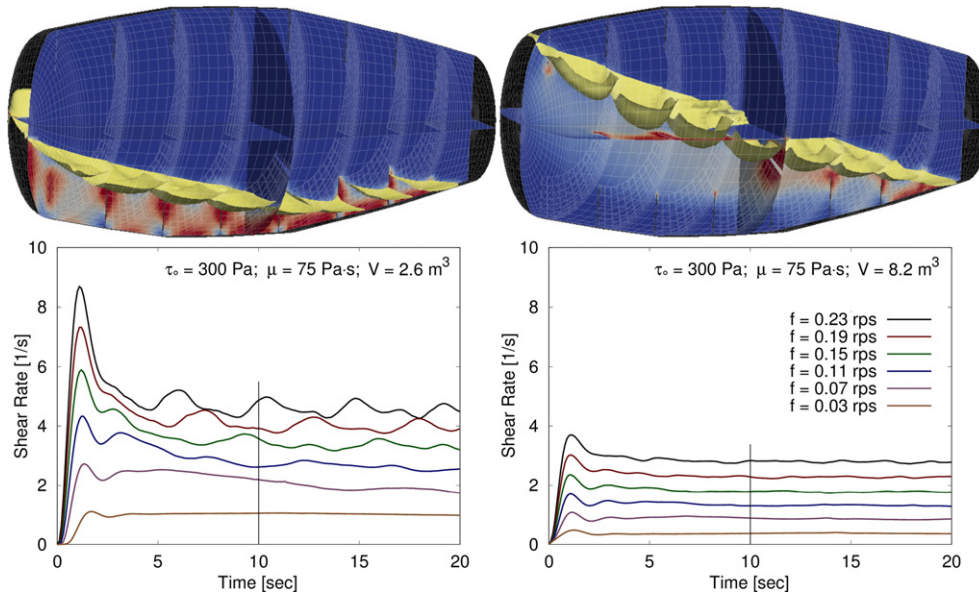
Fig. 3. Volume averaged shear rate $\bar{\dot{\gamma}}(t)$ by Eq. (8) plotted as a function of time t.
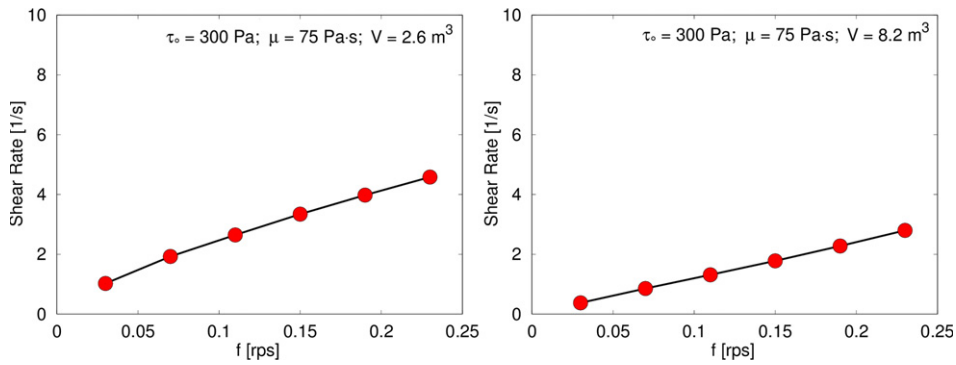

Fig. 4. Shear rate $\dot{\gamma}_t$ by Eq. (9) plotted as a function of drum speed f.
Source: Raw data $\bar{\dot{\gamma}}(t)$ is from Fig. 3

rate result because of this. However, increasing the simulation time in such manner that a complete revolution (or more) is achieved, did not change the outcome by any significance (see the lowest lines in Fig. 3). It did however increase the CPU cost and thus 20s of simulation time was maintained for most cases. Depending on the rheological values μ and τ_0, drum charge volume V and drum speed f, a single simulation of 20s took between 1 and 3 weeks using 4 CPU's. With more than 160 simulations, the computational requirement of this work is more than 150,000 CPU hours.

By time integrating Eq. (8) as shown with Eq. (9), only the latter part of the curves in Fig. 3 is utilized. The time integration starts at $t = 10$s as shown with the vertical lines in this figure. This choice (starting at $t = 10$s and not at $t = 0$s) is made due to the fact that equilibrium in shear rate $\bar{\dot{\gamma}}(t)$ is usually obtained at 10 s as demonstrated in Fig. 3.

$$\dot{\gamma}_t = \frac{1}{20\ \text{s} - 10\ \text{s}} \int_{10\ \text{s}}^{20\ \text{s}} \bar{\dot{\gamma}}(t)\, dt. \qquad (9)$$

Since all results presented in the remainder of this work are in terms of volume and time averaged shear rate $\dot{\gamma}_t$ by Eq. (9), this quantity

will simply be referred to as "shear rate". Calculating this shear rate for the data shown in Fig. 3, results in Fig. 4 and represents how the main results are presented in this work.
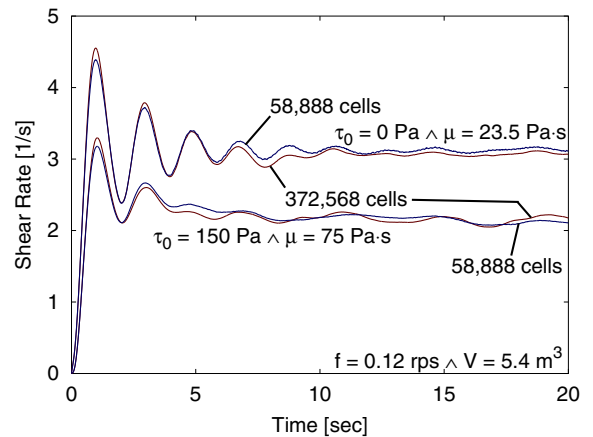

Fig. 5. Analysis of mesh independence in terms of volume averaged shear rate $\bar{\dot{\gamma}}(t)$ by Eq. (8).
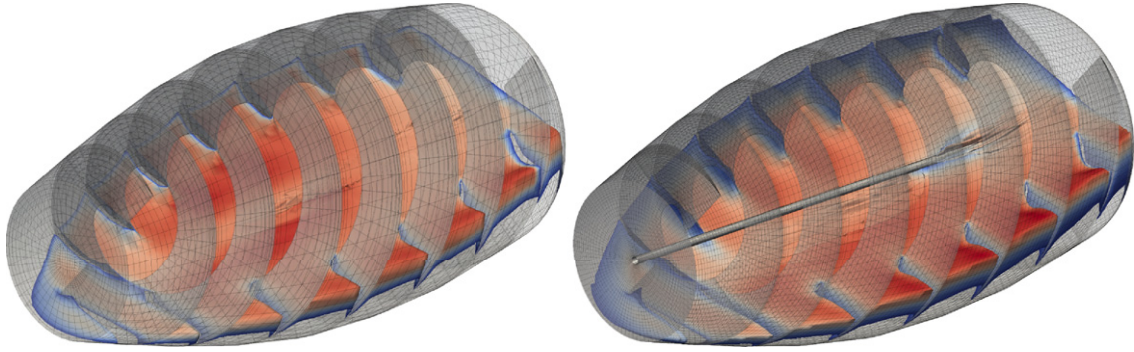
Fig. 6. To the left (58,888 cells) the center is meshed, while to the right (372,568 cells) cells are missing in the center, presented as a rod.

4. Results and discussion

4.1. Mesh independence

To investigate the mesh dependency of the numerical results, two very different mesh densities (or mesh resolutions) are used, namely 58,888 and 372,568 cells, already shown in Fig. 1. To make a quantifiable comparison, the analysis is done in terms of volume averaged shear rate $\bar{\dot{\gamma}}(t)$ calculated by Eq. (8). Two rheological cases are tested, namely with $\tau_0 = 0$ Pa and $\mu = 23.5$ Pa·s as a "low viscous case" and with $\tau_0 = 150$ Pa and $\mu = 75$ Pa·s as a "high viscous case". In either case, the drum speed is set to $f = 0.12$ rps and the drum charge volume to $V = 5.4$ m³. The outcome of this analysis is shown in Fig. 5. The low viscous results (for the two mesh densities) are shown by the two top lines, while high viscous results by the two bottom lines.

As shown in Fig. 5, the difference between the two mesh cases varies slightly as a function of time, but for the last 10 s of the analysis, the difference is in the order of 1% or less. Given the large difference in mesh density, a difference of 1% is very small, thus indicating good numerical quality.

Although the dimensions between the two mesh cases are identical (Fig. 1), there is a slight geometric difference. For the high resolution case, namely 372,568 cells, a rod is present in the center of the drum, shown in the right illustration of Fig. 6 (this applies also to the corresponding illustration in Fig. 1, but is not clearly apparent). Such rod is not present for the case of 58,888 cells (left illustration of Fig. 6), which is the geometrically correct case. To delete the rod, a special meshing technique has to be applied which is not easily implemented for non-uniform, skew and non-orthogonal cells that apply here. Because of the limited use of the high resolution mesh, no
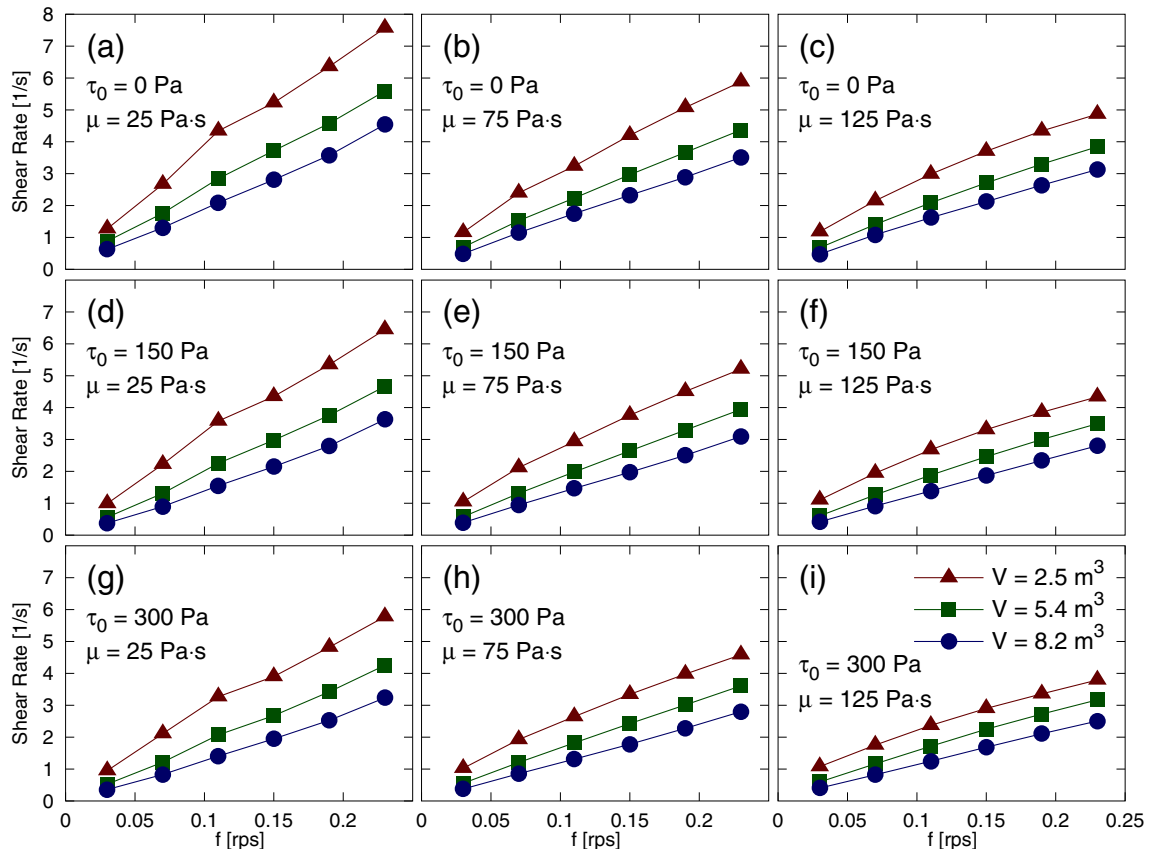

Fig. 7. Shear rate $\dot{\gamma}_t$ by Eq. (9) as a function of drum speed f for different conditions.

such center meshing was applied. The rod boundary condition is full-slippage for **U**, while for α_1 and p^* it is as previously reported. The point is that the difference between the two mesh cases (i.e. with and without rod) might also contribute to the difference shown in Fig. 5.

4.2. Shear rate as a function of drum speed

Fig. 7 shows plots of the shear rate $\dot{\gamma}_t$ by Eq. (9) as a function of drum rotational speed f. These results applies at different rheological cases, namely yield stress τ_0 and plastic viscosity μ. In each illustration, labeled from (a) to (i), are three graphs which apply to different drum charge volume V, nominally equal to 2.6m³, 5.4m³ and 8.2m³.

As to be expected, the outcome of Fig. 7 shows that the shear rate $\dot{\gamma}_t$ increases with increased drum rotational speed f. However, the increase does not have to be linear as shown in Fig. 7a, d and g. That is, for the combination of $V = 2.6$m³ and $\mu = 25$Pa·s, there is a small hump close to $f = 0.1$rps, which disappears with increased volume V and plastic viscosity μ.

From Fig. 7, it is clear that all the four quantities, drum speed f, drum charge volume V, yield stress τ_0 and plastic viscosity μ influence the shear rate $\dot{\gamma}_t$. As a proposal, the shear rate is modeled as shown with Eq. (10), with $\delta = 10$Pa. By using the Nelder and Mead simplex algorithm [55], its parameters are $p_1 = 53.6$Pa, $p_2 = 253$Pa·s, $p_3 = 37.6$m³ and $p_4 = 1.57$m³/s and found by simultaneous fitting all the data in Fig. 7.

$$\dot{\gamma}_t \approx \left(\frac{p_1}{\tau_0 + \delta} + \frac{p_2}{\mu} + \frac{p_3}{V} \right) f + \frac{p_4}{V}. \qquad (10)$$

As shown with Fig. 8, using the obtained parameters p_1, p_2, p_3 and p_4, Eq. (10) does not fully fit all the data points, clearly demonstrating the complexity of the flow involved. Despite of its inaccuracy,

this equation demonstrates the general trend of behavior. What is important to note is how the shear rate $\dot{\gamma}_t$ is controlled by the inverse of drum charge volume $1/V$, the inverse of yield stress $1/\tau_0$ and the inverse of plastic viscosity $1/\mu$. Thus, when considering the effect of volume V alone, the shear rate $\dot{\gamma}_t$ decreases in almost an exponential manner with volume. Also, the shear rate $\dot{\gamma}_t$ is very dependent on the rheological values τ_0 and μ, something which in general is an undesirable characteristics for rheometers, if the aim is to use the drum as such.

4.3. Shear rate as a function of drum charge volume

Fig. 9 shows plots of the shear rate $\dot{\gamma}_t$ by Eq. (9) as a function of drum charge volume V. These data consists of the same values as presented in Fig. 7, however only using the three cases of $f = 0.23$rps (Fig. 9a–c), $f = 0.11$rps (Fig. 9d–f) and $f = 0.03$rps (Fig. 9g–i).

From Fig. 9, it is clear that the shear rate decreases in almost exponential manner with increasing charge volume V, something which is reflected in Eq. (10). Thus, for a binder rich concrete where thixotropic thickening is an important contributor to workability loss, one solution would be to not fill the drum up to capacity (cf. Section 1.2). Rather, half full or less would be recommended since such could double the shear rate (i.e. double the agitation of the fresh concrete). This consideration would be especially important if the transport distance is long, e.g. several hours. Also, if it is indented to use the truck mixer as a ready mix plant (i.e. mix the concrete from its dry components and water), this would be especially important for the more difficult batches, like high powder concretes. Such example is shown in Fig. 10, which consists of the mixing of high performance concrete in the countryside in Iceland, too far away from available ready mix plants. Although the max concrete capacity was about 9m³ for the specific drum used, then based on the results in
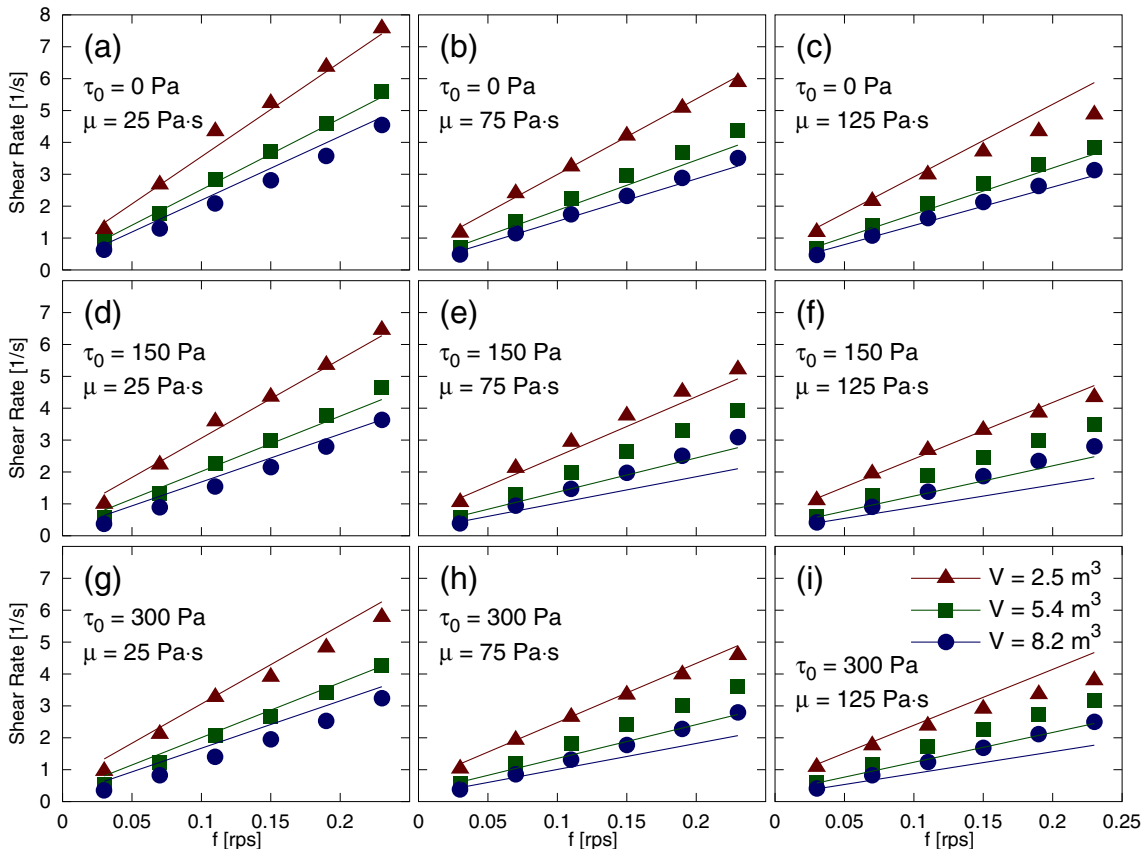

Fig. 8. Shear rate $\dot{\gamma}_t$ by Eq. (10) as a function of drum speed f plotted against the data points in Fig. 7.
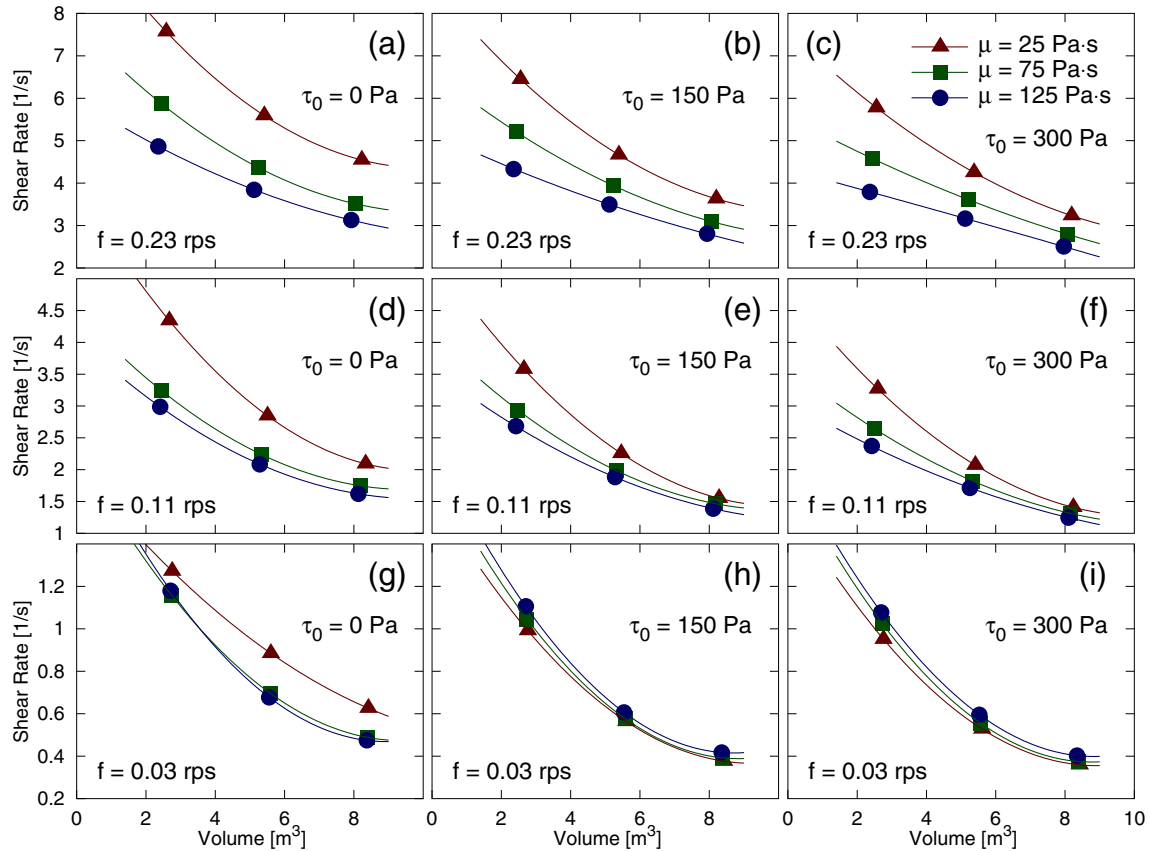
Fig. 9. Shear rate $\dot{\gamma}_t$ by Eq. (9) as a function of drum charge volume V.

Fig. 9, each batch consisted of only about 3m³ concrete. As mentioned above, mixing only such small quantity of concrete in each case was done to maximize the shear rate (i.e. agitation) and thus the mixing efficiency. This specific project was carried out by the Icelandic Road and Coastal Administration in cooperation with the Innovation Center Iceland and was very successful.

By closely examining the data points towards the "x-axis" in Fig. 9, one can see a slight variation in drum charge volume V between different rheological cases τ_0 and μ. This is because a small part of the concrete adheres to the internal surface of the drum. That is, part of the concrete sample becomes stuck on solid boundary on the atmospheric air side of the drum (i.e. the concrete which adheres to the steel surface). This coating concrete (on the air side) is not included in the volume integration of Eq. (8). The amount of concrete that becomes "lost" in this manner, has been shown to increase slightly with increasing yield stress τ_0, but more so with increasing plastic

Fig. 10. Batching of high performance concrete inside a truck mixer.

viscosity μ. Such behavior is also observed in reality, meaning that with high viscous concrete like a rich HPC, the material usually sticks to the surface almost like a chewy-gum, while much less so (or not at all) for a standard concrete that exhibits low (or very low) plastic viscosity μ.

In the above text, the nominal amount of concrete volume reported in this work, namely 2.6, 5.4 and 8.2m³, are average values, and the actual values can vary by few percents at most.

5. Conclusions

The shear rate has been analyzed inside a drum of a concrete truck mixer with the aim to better understand the effect of transport of fresh concrete, from the ready mix plant to the building site. In this context, a higher shear rate during transport implies a more flowable concrete at arrival, while a lower shear rate implies insufficient agitation, increased thixotropic rebuild and thus stiffer concrete during casting (see Section 1.3).

As to be expected, the outcome shows that the shear rate $\dot{\gamma}_t$ increases with increased drum rotational speed f (see Fig. 7). However in addition to this, the drum charge volume V, the yield stress τ_0 and the plastic viscosity μ all play an important role. That is, the shear rate $\dot{\gamma}_t$ is very dependent on rheological values τ_0 and μ, something what is in general an undesirable characteristics for rheometers, if the aim would be to use the drum as such.

To understand better how the shear rate $\dot{\gamma}_t$ is being affected, it was modeled with an algebraic equation by Eq. (10). Although this equation often gives approximate values (see Fig. 8), it demonstrates the general trend of behavior. What is important to note is how the shear rate $\dot{\gamma}_t$ is controlled by the inverse of drum charge volume $1/V$, the inverse of yield stress $1/\tau_0$ and the inverse of plastic viscosity $1/\mu$. Thus, when considering the effect of volume V alone, the

shear rate $\dot{\gamma}_t$ decreases in almost an exponential manner with it (see Fig. 9). If a lower shear rate condition is to be avoided, for example to avoid thixotropic buildup during a long transport distance of high performance concrete (HPC), then filling the drum up to its designated capacity (here, up to 9m^3), would not be advisable. Rather, half full or less would be recommended as such would in general double the shear rate and thus double the effective agitation of the concrete sample. This is especially important if it is indented to use the truck mixer as a ready mix plant (see Fig. 10) for an effective agitation during mixing.

Acknowledgments

References

[1] G.H. Tattersall, P.F.G. Banfill, The Rheology of Fresh Concrete, Pitman Books Limited, Great Britain, 1983. (Out of print but electronic copy available from P.F.G.Banfill@hw.ac.uk).

[2] N. Roussel, S. Staquet, L. D'Aloia Schwarzentruber, R. Le Roy, F. Toutlemonde, SCC casting prediction for the realization of prototype VHPC-precambered composite beams, Mater. Struct. 40 (9) (2007) 877–887.

[3] L.N. Thrane, Form Filling With Self-Compacting Concrete, Department of Civil Engineering, Technical University of Denmark. 2007. Ph.D. thesis.

[4] J. Spangenberg, N. Roussel, J.H. Hattel, H. Stang, J. Skocek, M.R. Geiker, Flow induced particle migration in fresh concrete: theoretical frame, numerical simulations and experimental results on model fluids, Cem. Concr. Res. 42 (2012) 633–641.

[5] A. Gram, J. Silfwerbrand, B. Lagerblad, Obtaining rheological parameters from flow test – analytical, computational and lab test approach, Cem. Concr. Res. 63 (2014) 29–34.

[6] K. Vasilic, W. Schmidt, H.C. Kuhne, F. Haamkens, V. Mechtcherine, N. Roussel, Flow of fresh concrete through reinforced elements: experimental validation of the porous analogy numerical method, Cem. Concr. Res. 88 (2016) 1–6.

[7] N. Roussel, A. Gram, M. Cremonesi, L. Ferrara, K. Krenzer, V. Mechtcherine, S. Shyshko, J. Skocec, J. Spangenberg, O. Svec, L.N. Thrane, K. Vasilic, Numerical simulations of concrete flow: a benchmark comparison, Cem. Concr. Res. 79 (2016) 265–271.

[8] O. Svec, J. Skocek, H. Stang, M.R. Geiker, N. Roussel, Free surface flow of a suspension of rigid particles in a non-Newtonian fluid: a lattice Boltzmann approach, J. Non-Newtonian Fluid Mech. 179-180 (2012) 32–42.

[9] V. Mechtcherine, A. Gram, K. Krenzer, J.H. Schwabe, S. Shyshko, N. Roussel, Simulation of fresh concrete flow using Discrete Element Method (DEM): theory and applications, Mater. Struct. 47 (2014) 615–630.

[10] N. Roussel, A. Gram (Eds.), Simulation of Fresh Concrete Flow, State-of-the Art Report of the RILEM Technical Committee 222-SCF, Springer.2014,

[11] K. Krenzer, J. Martin, U. Palzer, Development of a Truck Mixer Simulator on a Laboratory Scale Using CAD and Simulation, CPI-Worldwide, 2014. Issue 1.

[12] P.F.G. Banfill, D.S. Swift, The effect of mixing on the rheology of cement-based materials containing high performance superplasticizers, Ann. Trans. Nordic Rheol. Soc. (2004) vol. 12.

[13] J. Orban, P. Parcevaux, D. Guillot, Influence of shear history on the rheological properties of oil well cement slurries, Proc. 8th Int. Congress on the Chemistry of Cement, vol. 6, 1986.

[14] P.F.G. Banfill, Structural breakdown and the rheology of cement mortar, Proc. XIth Int. Congress on Rheology, Elsevier. 1992.

[15] J.E. Wallevik, Thixotropic investigation on cement paste: experimental and numerical approach, J. Non-Newtonian Fluid Mech. 132 (2005) 86–99.

[16] N. Roussel, A thixotropy model for fresh fluid concretes: theory, validation and applications, Cem. Concr. Res. 36 (2006) 1797–1806.

[17] J.E. Wallevik, Rheological properties of cement paste: thixotropic behavior and structural breakdown, Cem. Concr. Res. 39 (2009) 14–29.

[18] J.E. Wallevik, Particle flow interaction theory - thixotropic behavior and structural breakdown, Inproceedings of 36th Conference on Our World of Concrete and Structures, 14–16th August, Singapore, 2011.

[19] H.G. Weller, G. Tabor, H. Jasak, C. Fureby, A. tensorial approach to computational continuum mechanics using object-oriented techniques, Comput. Phys. 12 (1998) 620–631.

[20] E. Berberovic, Investigation of Free-Surface Flow Associated With Drop Impact: Numerical Simulations and Theoretical Modeling, Technische Universitat Darmstadt, Darmstadt, 2010. Ph.D. thesis.

[21] D. Gerlach, G. Tomar, G. Biswas, F. Durst, Comparison of volume-of-fluid methods for surface tension-dominant two-phase flows, Int. J. Heat. Mass. Tran. 49 (2006) 740–754.

[22] C.W. Hirt, B.D. Nichols, Volume of fluid (VOF) method for the dynamics of free boundaries, J. Comput. Phys. 39 (1) (1981) 201–225.

[23] V.R. Gopala, B.G.M. van Wachem, Volume of fluid methods for immiscible-fluid and free-surface flows, Chem. Eng. J. 141 (2008) 204–221.

[24] J. Klostermann, K. Schaake, R. Schwarze, Numerical simulation of a single rising bubble by VOF with surface compression, Int. J. Numer. Meth. Fluids 71 (8) (2013) 960–982.

[25] K. Kissling, J. Springer, H. Jasak, S. Schutz, K. Urban, M. Piesche, A coupled pressure based solution algorithm based on the volume-of-fluid approach for two or more immiscible fluids, in: J.C.F. Pereira, A. Sequeira (Eds.), Fifth European Conference on Computational Fluid Dynamics, ECCOMAS CFD 2010, Lisbon, Portugal, June 2010.

[26] D.L. Youngs, An interface tracking method for a 3D Eulerian hydrodynamics code, Technical Report AWRE/44/92/35, Atomic Weapons Research Establishment. 1987.

[27] W. Noh, P. Woodward, SLIC (simple line interface calculation), in: A.I. van de Vooren, P. Zandbergen (Eds.), Proceedings of the Fifth International Conference on Fluid Dynamics, Lecture Notes in Physics vol. 59, Springer-Verlag, Berlin, 1976,

[28] T. Waclawczyk, T. Koronowicz, Comparison of CICSAM and HRIC high-resolution schemes for interface capturing, J. Theor. Appl. Mech. 46 (2) (2008) 325–345.

[29] O. Ubbink, Numerical Prediction of Two Fluid Systems With Sharp Interfaces, Imperial College of Science, Technol. Med., 1997. Ph.D. thesis.

[30] O. Ubbink, R.I. Issa, Method for capturing sharp fluid interfaces on arbitrary meshes, J. Comput. Phys. 153 (1999) 26–50.

[31] S. Muzaferija, M. Peric, P. Sames, T. Schelin, A two-fluid Navier-Stokes solver to simulate water entry, Proc. Twenty-Second Symposium on Naval Hydrodynamics, 1998.

[32] H.G. Weller, Derivation modelling and solution of the conditionally averaged two-phase flow equations, Technical Report TR/HGW/02, Nabla Ltd. 2002.

[33] H. Rusche, Computational Fluid Dynamics of Dispersed Two-Phase Flows at High Phase Fractions, Department of Mechanical Engineering, Imperial College of Science, Technology & Medicine, London, 2002. Ph.D. thesis.

[34] J.P. Boris, D.L. Book, Flux-corrected transport, I. SHASTA, a fluid transport algorithm that works, J. Comput. Phys. 11 (1973) 38–69.

[35] S.T. Zalesak, Fully multidimensional flux-corrected transport algorithms for fluids, J. Comput. Phys. 31 (1979) 335–362.

[36] S.M. Damian, An Extended Mixture Model for the Simultaneous Treatment of Short and Long Scale Interfaces, Facultad de Ingenieria y Ciencias Hidricas, Universidad Nacional del Litoral, 2013. Ph.D. thesis.

[37] G.E. Mase, Schaums Outline Series: Theory and Problems of Continuum Mechanics, McGraw-Hill Inc., USA, 1970.

[38] L.E. Malvern, Introduction to the Mechanics of Continuous Medium, Prentice-Hall Inc., New Jersey, 1969.

[39] J.U. Brackbill, D.B. Kothe, C. Zemach, A continuum method for modelling surface tension, J. Comput. Phys. 100 (1992) 335–354.

[40] F.P. Karrholm, Rhie-Chow Interpolation in OpenFOAM, Department of Applied Mechanics, Chalmers Univesity of Technology, Goteborg, Sweden, 2006.

[41] R.I. Tanner, K. Walters, Rheology: An Historical Perspective, Elsevier Science B.V., Netherlands, 1998.

[42] H.A. Barnes, J.F. Hutton, K. Walters, An Introduction to Rheology, Elsevier Science B.V., Netherlands, 1989.

[43] M. Bercovier, M. Engelman, A finite element method for incompressible non-Newtonian flows, J. Comput. Phys. 36 (1980) 313–326.

[44] A.J. Taylor, S.D.R. Wilson, Conduit flow of an incompressible, yield-stress fluid, J. Rheol. 41 (1) (1997) 93–101.

[45] G.R. Burgos, A.N. Alexandrou, V. Entov, On the determination of yield surfaces in Herschel-Bulkley fluids, J. Rheol. 43 (3) (1999) 463–483.

[46] J.E. Wallevik, Rheology of Particle Suspensions - Fresh Concrete, Mortar and Cement Paste With Various Types of Lignosulfonates, Department of Structural Engineering The Norwegian University of Science and Technology, Trondheim, Norway, 2003, Ph.D. thesis. http://ntnu.diva-portal.org.

[47] J.E. Wallevik, Minimizing end-effects in the coaxial cylinders viscometer: viscoplastic flow inside the ConTec BML Viscometer 3, J. Non-Newtonian Fluid Mech. 155 (2008) 116–123.

[48] D. Feys, J.E. Wallevik, A. Yahia, K.H. Khayat, O.H. Wallevik, Extension of the Reiner-Riwlin equation to determine modified Bingham parameters measured in coaxial cylinders rheometers, Mater. Struct. 46 (2013) 289–311.

[49] J.E. Wallevik, K. Krenzer, J.H. Schwabe, Numerical errors in CFD and DEM modeling, in: N. Roussel, A. Gram (Eds.), Simulation of Fresh Concrete Flow, Springer, Netherlands, 2014.

[50] ANSYS FLUENT 6.3 User's Guide 2006, ANSYS Inc., USA, 2006.

[51] M.L. Salby, Fundamentals of Atmospheric Physics, Academic Press. 1996.

[52] H.K. Versteeg, W. Malalasekera, An Introduction to Computational Fluid Dynamics - The Finite Volume Method, 2nd Ed. ed., Pearson Education Limited, England, 2007.

[53] OpenFOAM User Guide, Version 2.3.1, The OpenFOAM Foundation. 2014.

[54] J.E. Wallevik, Effect of the hydrodynamic pressure on shaft torque for a 4-blades vane rheometer, Int. J. Heat Fluid Flow 50 (2014) 95–102.

[55] J.A. Nelder, R. Mead, A simplex method for function minimization, Computer. J. 7 (1965) 308–313.